

Janus graphene nanoribbons with a single ferromagnetic zigzag edge

Shaotang Song^{1,9}, Yu Teng^{1,7,9}, Weichen Tang^{2,4,9}, Zhen Xu^{3,9}, Yuanyuan He¹, Jiawei Ruan^{2,4}, Takahiro Kojima³, Wenping Hu^{7,8}, Franz J Giessibl⁵, Hiroshi Sakaguchi*³, Steven G Louie*^{2,4}, Jiong Lu*^{1,6}

¹Department of Chemistry, National University of Singapore, 3 Science Drive 3, Singapore 117543, Singapore.

²Department of Physics, University of California, Berkeley, CA94720, USA.

³Institute of Advanced Energy, Kyoto University, Uji, Kyoto 611-0011, Japan.

⁴Materials Sciences Division, Lawrence Berkeley National Laboratory, Berkeley, CA 94720, USA.

⁵Institute of Experimental and Applied Physics, University of Regensburg, 93053 Regensburg, Germany.

⁶Institute for Functional Intelligent Materials, National University of Singapore, Singapore, Singapore.

⁷Joint School of National University of Singapore and Tianjin University, International Campus of Tianjin University, Fuzhou 350207, China.

⁸Tianjin Key Laboratory of Molecular Optoelectronics, Department of Chemistry, School of Science, Tianjin University, Tianjin, 300072 China.

⁹These authors contribute equally: Shaotang Song, Yu Teng, Weichen Tang, Zhen Xu
E-mail: sakaguchi@iae.kyoto-u.ac.jp (H.S.); sglouie@berkeley.edu (S.G.L.);
chmluj@nus.edu.sg (J.L)

Abstract

Topological design of π -electrons in zigzag-edged graphene nanoribbons (ZGNRs) leads to a wealth of magnetic quantum phenomena and exotic quantum phases.¹⁻⁹ Symmetric ZGNRs typically exhibit antiferromagnetically coupled spin-ordered edge states.^{1,2,6} Eliminating cross-edge magnetic coupling in ZGNRs not only enables the realization of a new class of ferromagnetic quantum spin chains,¹⁰ enabling the exploration of quantum spin physics and entanglement of multiple qubits in the 1D limit,^{3,11} but also establishes a long-sought carbon-based ferromagnetic transport channel, pivotal for ultimate scaling of GNR-based quantum electronics.^{1-3,6,9,12} However, designing such GNRs entails overcoming daunting challenges, including simultaneous breaking of structural and spin symmetries, and designing elegant precursors for asymmetric fabrication of reactive zigzag edges. Here, we report a general approach for designing and fabricating such ferromagnetic GNRs in the form of Janus GNRs (JGNRs) with two distinct edge configurations. Guided by Lieb's theorem and topological classification theory,¹³⁻¹⁵ we designed two JGNRs by asymmetrically introduced a topological defect array (TDA) of benzene motifs to one zigzag edge, while keeping the opposing zigzag edge unchanged. This breaks structural symmetry and creates a sublattice imbalance within each unit cell, initiating a spin symmetry breaking. Three 'Z-shape' precursors are designed to fabricate one parent ZGNR and two JGNRs with an optimal lattice spacing of TDA for a complete quench of the magnetic edge states at the "defective" edge. Characterization *via* scanning probe microscopy/spectroscopy and first-principles density functional theory (DFT) confirms the successful fabrication of JGNRs with ferromagnetic ground state delocalised along the pristine zigzag edge. Realizing such JGNRs not only expands the design space for precise engineering of exotic quantum magnetism but also enables the creation of robust spin centers as promising qubit platforms through bottom-up assembly. Furthermore, it allows for fabricating 1D spin-polarized transport channels with tunable bandgaps for carbon-based spintronics in the 1D limit.

Introduction

The term "Janus" has been adopted to denote materials that exhibit different properties on two opposing sides or faces.^{16,17} In the realm of 2D materials, creating asymmetric Janus materials by breaking out-of-plane mirror symmetry, provides an attractive route for engineering novel properties and functionalities such as enhanced valley spin splitting, out-of-plane piezoelectricity and second harmonic generation.¹⁸⁻²¹ Reducing the dimension of Janus materials from 2D to 1D systems with two different edge structures/topologies (hence properties), especially those with asymmetric zigzag edges in JGNRs, creates new opportunities for the realization of 1D ferromagnetic quantum spin chains and the assembly of multiple qubits. It also enables the creation of ferromagnetic transport channel in the 1D limit,^{22,23} which can carry completely spin polarized current without applying in-plane electric field,²⁴ strain²⁵ or chemical functionalizations,^{26,27} as required for conventional ZGNRs. However, the rational design of such novel JGNRs requires the simultaneous breaking of their structural and spin symmetries. This task is even more challenging than fabricating symmetric ZGNRs, which is notoriously difficult due to the high reactivity of zigzag edges combined with the challenges in intricate design and synthesis of precursors. To date, only two symmetric ZGNRs have been reported, both based on the 'U-shape' precursor design. Moreover, the width of the obtained ZGNRs is limited to six carbon zigzag chain across the ribbon, namely, 6-ZGNR.^{1,2}

The design principle for JGNRs

Our strategy for creating such JGNRs involves decorating one zigzag edge of ZGNRs with a topological "defect" array (termed as TDZ edge), while keeping the other zigzag edge unchanged. Guided by this principle, we introduce a periodic array of benzene motifs attached to the TDZ edge to break structural symmetry and to create a sublattice imbalance within each unit cell ($\Delta N = 1$), leaving one unpaired radical site in each unit cell (Fig. 2).^{13,28} As a result, this introduces magnetism in line with Lieb's theorem, initiating the spin symmetry breaking in this system.²⁹⁻³¹ To effectively quench the spin at the TDZ edge and maintain a single ferromagnetic edge-state band at the zigzag edge, we show that the key is to determine the optimal spacing (denoted as m , $m=1, 2, 3$, etc) between periodic benzene rings

at the TDZ edge that maximally disrupts the edge states. To achieve this, we applied the topological classification using chiral symmetry developed in Ref. 15. In 1D bipartite lattices such as GNRs, because of the negligible second-nearest-neighbour interactions, chiral symmetry is satisfied, leading to a Z -classification of their electronic topological phases with a conventional Z index (with Z an integer value).¹⁵ As the Z index is 0 for vacuum, from bulk-interface correspondence, the number of topological end states are dictated by the absolute value of the Z index.

For our design principle, we note the important correspondence here that the *edge* of a ZGNR can be viewed as the *end* of an armchair-edged GNR (AGNR) in the large width limit. This means the existence and characteristics of the *topological edge states* of a defective ZGNR edge are the same as those of the *topological end states* of a large-width AGNR with a similar defective structure at its end. When examining the topological behavior of the end of an AGNR, the Z index can be expressed in a straightforward form¹⁵:

$$Z = N_{\text{notco}} - \left\lfloor \frac{N}{3} \right\rfloor \quad (1)$$

where N represents the total number of rows of carbon atoms forming the width of the AGNR, and N_{notco} is the number of rows of atoms with unconnected carbon pairs (Fig. S1). The topless brackets in Eq. (1) denote the floor function, which takes the largest integer less than or equal to the value within the brackets.

Fig. 1a shows a family of JGNRs with different spacing of m as defined in Fig. 1b. For conceptual understanding of the topological states, we consider the edge of a finite-length ZGNR as an end of an AGNR consisting of L identical repeated units along its width, with L to be taken to the large limit and equal to a multiple integer of 3. Since there is a total number of L repeated units in each defective ends, the overall count of the number of rows of carbon atoms for the *associated* AGNR is (by construction) given by $N = 2(m + 1)L$ where m is the number of missing benzene ring as shown in Fig. 1a. For a specific defective edge with a given m , $N_{\text{notco}} = mL$, and the corresponding chiral phase index (CPI) Z (which dictates the number of topological states) is $Z_{TDZ} = \frac{m-2}{3}L$ using the Jiang-Louie formula¹⁵ given in Eq. (1). In the case of the non-defective end (i.e., the normal zigzag edge), $N_{\text{notco}} = (m+1)L$, and the corresponding CPI is $Z_{zig} = \frac{m+1}{3}L$ (a detailed analysis can be found in the supplemental material). Moreover, according to Lieb's theorem, when considering the electron spin degree

of freedom, the topological end/edge states become spin-polarized, forming a magnetic ground state. As illustrated in Fig. 1b, the sublattice imbalance (difference in numbers of atoms of the A and B sublattice of graphene) for all JGNRs is $\Delta NL = L$ (since $\Delta N=1$ is the sublattice imbalance per unit cell as defined in Fig. 1). Thus, the ground state of the system consists of $\frac{m-2}{3}L$ spin-up topological states localized at the TDZ edge of JGNRs (or viewed as the end of the finite AGNR) and $\frac{m+1}{3}L$ spin-down topological states localized at the zigzag edge at the other end. (Our *ab initio* density functional theory (DFT) calculations that validate our argument numerically can be found in the Supplemental Information, Fig. S1-S3).

With the above topological CPI analysis, we reach the following remarkable conclusion without employing any detailed calculations: The sign of the quantity R , defined as the negative of the ratio between the CPI of the two edges $R = -\frac{Z_{TDZ}}{Z_{zig}} = -\frac{m-2}{m+1}$, determines the magnetic ordering of the JGNRs (Fig. 1c). For $m = 1$ (with $R > 0$), both edges of JGNR adopt the same spin alignment but with different magnitude, giving rise to a ferromagnetic state. In contrast, for $m > 2$ (where $-1 < R < 0$), the two edges of JGNR exhibit different spin configurations with varying magnitude, resulting in a ferrimagnetic order. Notably, when $m = 2$ ($R = 0$), no edge state exists at the TDZ edge, leading to the formation of a ferromagnetic ground state localized exclusively at the zigzag edge. The density of states for the $m = 2$ case (Fig. 1d) is in contrast to that of the symmetric ZGNRs with antiferromagnetically coupled edge states. In this framework, the conventional symmetric ZGNRs can be viewed as an extreme scenario with $m = \infty$ (with $R = -1$), where the perturbation of the infinitely-spaced benzene rings becomes zero. Therefore, by varying the parameter m associated with the periodicity of topological “defects” on one edge, our theory predicts the emergence of different magnetic ground states with different cross-edge couplings in JGNR, which is unattainable in symmetric ZGNRs (Fig. 1a).

Since ($m = 2$)-JGNR is predicted to feature the unique ferromagnetic ground state with a single ferromagnetic zigzag edge, our study focuses on the synthesis and investigation of this type of JGNRs. Here, we used the nomenclature (n, m)-JGNRs to describe the specific JGNRs, where n refers to the number of carbon zigzag chain forming the width of the symmetric ZGNR and m denotes the benzene ring spacing at the TDZ edge, as defined above.

Specifically, we target to fabricate the (4,2)- and (5,2)-JGNRs (Fig. 2), which have different widths, and the parent 5-ZGNR (Fig.3) (which can also be viewed as the corresponding (5, ∞)-JGNR) to experimentally validate our topological theory predictions and our design principle.

Precursor design for on-surface synthesis of JGNRs

To achieve the on-surface synthesis of the two ($n,m = 2$)-JGNRs, we employ a Z-shaped molecular precursor design for the asymmetric fabrication, in contrast with the U-shaped precursor for the on-surface synthesis of the 6-ZGNR reported previously.³²⁻³⁵ The Z-shaped precursor comprises of two independent branch moieties that are interconnected by a single C-C bond. At the termini of the branches, two bromine atoms are strategically positioned as connection sites for thermally induced aryl-aryl coupling. The Z-shaped precursor design also allows for the independent modification of individual branches, facilitating a separate control over the two edge geometries of the resulting JGNRs. Utilizing methylphenanthrene groups for both branches (precursor **3** in Fig. 3) yields two identical zigzag edges, corresponding to the conventional 5-ZGNR. Intriguingly, substituting one of the methylphenanthrene groups to a polyphenyl group results in the modification of one of the zigzag edges to our target TDZ edge with periodically decorated benzene rings (with a spacing of $m = 2$). Additionally, adjusting the length of the polyphenyl groups from biphenyl to triphenyl (precursor **1** and **2** in Fig. 2) enables the modulation of the width of the JGNRs from $n=4$ to $n=5$.

The precursors were successfully obtained *via* multi-step organic synthesis (see Supplementary Information) and then separately deposited onto a clean Au(111) surface under ultrahigh vacuum (UHV) using a Knudsen cell evaporator. Stepwise annealing of the precursor decorated surfaces induces polymerization and cyclodehydrogenation reactions to yield the corresponding (4,2)- and (5,2)-JGNRs (Fig. 2) and 5-ZGNR (Fig. 3). The yield of all the GNRs is relatively low within the annealing temperature window and conditions we have examined. This is primarily due to the flexible backbone of the corresponding polymers, which undergo random cyclodehydrogenation reactions during the thermal annealing process. In addition, the asymmetric precursors **1** and **2** can exhibit different polymerization manners, namely head-to-tail, and head-to-head (tail-to-tail). If polymerization proceeds in a head-to-head (tail-to-tail) configuration, then the resulting GNRs will feature alternative cove and gulf regions on both edges.^{33,34} Here, we focus on the investigation of the targeted JGNRs

through the head-to-tail polymerization. The topographic STM images of both (4,2)-JGNR and (5,2)-JGNR reveal a characteristic height profile and morphology featuring bright lobes at the intact zigzag edge and larger protrusions at the TDZ edge, corresponding to the position of periodically-spaced benzene rings. The bond-resolved scanning tunnelling microscopy (BR-STM) images of both JGNRs acquired at -10 mV using a CO-functionalized tip exhibit the corrugated hexagon-like rings in the centre and distorted lobe features along the edges, which are presumably attributed to the perturbations induced by the electronic states of the JGNRs in the vicinity of Fermi level (E_F).^{36,37} In contrast, the BR-STM image of 5-ZGNR acquired at 10 mV using a CO-functionalized tip clearly resolves the characteristic hexagon patterns in the backbone, indicating an absence of electronic states near E_F .

To better resolve the backbone framework of both JGNRs, we further conducted the qPlus sensor-based non-contact atomic force microscopy (nc-AFM) images, which relies on monitoring the resonance frequency shift of an oscillating quartz force sensor as the CO functionalized tip scans over the sample in the Pauli repulsive regime.^{38,39} The achieved resolution directly confirms the different edge morphologies correspond to the expected JGNRs as defined by the precursor design. It is noted that the outer benzene rings on the TDZ edge appear flattened along the ribbon and larger in size than the ones in the backbone, while the outer rings at the intact zigzag edges appear stretched in the direction perpendicular to the ribbon. Such a different appearance of hexagons at different edges of JGNRs is presumably due to varying degrees of CO-tip bending effect due to different edge topologies. All these results prove the success of the Z-shape precursor design strategy for the synthesis of both JGNRs and 5-ZGNR.

Scanning tunnelling spectroscopy of the GNRs.

Previous studies revealed magnetic edge states cannot be directly observed in the wider 6-ZGNR and N-doped 6-ZGNR when sitting on Au(111), because they coupled strongly to the metal substrate.^{1,2} Compared to 6-ZGNR, both 5-ZGNR and the two JGNRs have a narrower ribbon width, thus leading to a more rigid backbone that could prevent a strong structural downward bending and electronic coupling with substrate.⁴⁰ Our differential conductance (dI/dV) spectroscopic measurements acquired over both 5-ZGNR and JGNRs combined with theoretical calculations confirm that magnetic edge states can survive on Au(111) for these narrower ribbons (Fig. 3). dI/dV spectrum obtained at the edge of 5-ZGNR show three

distinct peaks located at 750 ± 18 mV (peak A), -225 ± 5 mV (peak B), and -470 ± 7 mV (peak C), yielding an apparent experimental band gap of $\Delta E_{exp} = 980 \pm 19$ meV (Fig. 3c and Fig. S5). The experimental gap of 5-ZGNR is smaller than that of the 6-ZGNR (1.5 eV) placed on top of a monolayer NaCl island. Such behaviour is likely attributed to the screening effect of the metal substrate in reducing the quasiparticle energies and band gaps of reduced dimensional systems.⁴¹⁻⁴⁴ The dI/dV maps recorded at the biases corresponding to these three peak energies reveal the characteristic lobe features predominately located at both zigzag edges, demonstrating reproducible patterns in the DFT-calculated local density of states (LDOS) maps of each of the frontier band states (Figure 3d-f).

As shown in Fig. 4a, dI/dV spectrum taken over the zigzag edge of (4,2)-JGNR also reveals three noticeable features located at 560 ± 7 mV (peak A), 48 ± 5 mV (peak B) and -492 ± 5 mV (peak C), which yields an apparent band gap of $\Delta E_{exp} = 512 \pm 9$ meV for (4,2)-JGNR. However, peak C is absent in the dI/dV curve taken over the additional benzene ring of the TDZ edge. The most pronounced peak B spans across E_F , which is tentatively assigned as the partially-emptied top of the valence band (spin down and localized mainly along the intact zigzag edge) arising from the charge transfer due to the work function difference between GNR and Au(111). dI/dV image (Fig. 4c) acquired at the energy positions of peak B shows a petal-shaped feature on the zigzag edge and flower-shaped features distributed on the entire backbone of the (4,2)-JGNR. In contrast, the spatial distribution of other two peaks of the (4,2)-JGNRs reveal similar characteristic zigzag lobe features predominately or exclusively located at the intact zigzag edges for peak A and peak C, respectively (Fig. 4b, 4d, and Fig. S7). Similarly (Fig. 4j and Fig. S6), dI/dV spectrum of (5,2)-JGNR also reveals three peak structures centered at 417 ± 8 mV (peak A), 11 ± 3 mV (peak B) and -500 ± 13 mV (peak C), which yields a smaller apparent band gap of $\Delta E_{exp} = 406 \pm 9$ meV. Compared to (4,2)-JGNR, all the states observed in (5,2)-JGNR experience a slight downward shift in energy, but their spatial distribution patterns in the dI/dV maps are rather similar (Fig. 4k-4m, and Fig. S8).

***Ab initio* calculation of JGNRs electronic structures**

A direct capture of spectroscopic features and their wave function patterns of electronic states for both 5-ZGNRs and the two JGNRs suggest a relatively weak coupling of the ribbons with

the Au(111) substrate. We thus conducted *ab initio* density functional theory (DFT) calculations within the local spin density approximation (LSDA) to calculate the spin-polarized electronic structure for the free-standing ZGNRs and JGNRs. Our first-principles results offer quantitative evidence that the 5-ZGNR and two JGNRs synthesized on Au(111) all maintain their intrinsic magnetic edge states. Panels in Fig. 3g-3i present the calculated LDOS maps acquired at the energies corresponding to peak A' (conduction band minimum), peak B' (valence band maximum), and peak C' (the valence band states near the Brillouin zone edge X) of the freestanding 5-ZGNR, respectively. The distinctive pattern and relative contrast of protrusions lining the edges of 5-ZGNRs observed in experimental dI/dV images (Fig. 3d-f) are well reproduced in the corresponding LDOS maps (Fig. 3g-i). The DFT-calculated band structure (Fig. 3l) reveals that the valence band (VB) is more dispersive than the conduction band (CB) in the region of around one-third of Brillouin zone edge near the X point, forming a double-peak structure in the DOS spectrum due to the van Hove singularities at the VB maximum away from X (peak B') and at the X point (peak C'). In contrast, the bottom of the CB is significantly flattened in this region of Brillouin zone, forming only one peak in the DOS spectrum (peak A'). Similar behaviour in electronic band dispersion has been observed in 6-ZGNR in previous study³. It is also noted that the experimental gap (980 ± 35 meV) derived from dI/dV spectra is larger than that of the DFT-calculated one (330 meV). Given DFT's tendency to significantly underestimate quasiparticle bandgaps⁴⁵ even when factoring in the screening effects of the underlying Au substrate, it is not surprising that the DFT value is smaller than the experimentally observed gap. Nevertheless, the relative energy positions of the three electronic peaks near E_F , along with their corresponding LDOS, are in good agreement with experimental data. In addition, our *ab initio* calculations on 5-ZGNR reveal that an antiferromagnetic alignment of spins across the ribbon width between ferromagnetically ordered edge states is favored as the ground state over both the non-magnetic or a fully ferromagnetic configurations, as illustrated in the spin density plot (the inset of Fig. 3l; note that the absolute spin orientation is arbitrary due to negligible spin-orbit interactions in carbon systems).

In striking contrast, our DFT calculations directly demonstrate that the ground state for both the JGNRs studied is ferromagnetic, with ferromagnetic spin ordered edge states located *only* at the intact zigzag edge (inset of Fig. 4h and 4q). As seen in Fig. 4i and 4r, the bands are spin-polarized and there is an imbalance of the occupied spin-down vs spin-up polarized bands. In particular, the two bands near E_F (the lowest CB and the highest VB) bracketing the

E_F are edge-state bands and show a splitting energy gap of 0.21 eV and 0.19 eV for the (4,2)-JGNR and (5,2)-JGNR, respectively. Similar to the 5-ZGNR, the highest VB of both JGNRs is more dispersive than the lowest CB, with the former forming a double-peak feature (B' and C') in the DOS spectrum due to the presence of van Hove singularities at the Γ and the X point of the Brillouin zone. Conversely, the first CB is notably flattened, forming a sharp peak (A') in the DOS. Despite a variation in their widths, the calculated LDOS patterns of these peak states remain similar, and correspond well with the experimental dI/dV maps. Since the physical properties of JGNRs near the E_F are dominated by these edge states, variations in the JGNR's width would only quantitatively change the low-energy physics. According to our prediction on the $(n,m=2)$ -JGNR, if the width of the JGNRs goes to infinity, almost all the states in the lowest CB and the highest VB would be localized at the zigzag edge. However, more bands will appear near the Fermi level.

Previous tight binding calculations on *pristine* ZGNRs indicate a k -dependent localization length of the states at the zigzag edge, with states being more localized when closer to the X point of the ZGNR Brillouin Zone.⁵ Since the edge states of $(n,m=2)$ -JGNRs can be viewed as band-folded states of ZGNR, for the peak originating from states near the X point of the highest VB of JGNR (peak C'), they all originate from states near X point of the *pristine* ZGNR. The localization length of those states are small compared to the width of JGNRs, so the theoretical LDOS pattern shows a localized pattern at the zigzag edge (see Fig. 4g and 4p). In contrast, for states closer to the Γ point (at near 1/3 way from X to Γ or beyond), the localization length exceeds the width of JGNRs. The corresponding theoretical LDOS pattern (peak B') shows a delocalized pattern throughout the ribbon width (Fig. 4f and 4o). For the peak formed by the CB (peak A'), it comprises states from the entire Brillouin zone, and the LDOS pattern can be viewed as a mixture of the previous two patterns (Fig. 4e and 4n). We note that in the experiment, peak B located at near E_F for both JGNRs. This is due to the fact that the work function difference between our GNRs (~ 4.5 eV) and Au(111) (~ 5.3 eV) entails electron transfer from the JGNRs to the substrate, which lifts the valence band maximum upwards to the Fermi level.

Conclusion

Guided by our topological classification theory, the successful bottom-up synthesis of atomically precise JGNRs with a single ferromagnetic zigzag edges offers a rich platform not only for exploring novel quantum spin physics but also for its technological relevance. Such

JGNRs could serve as a model system to realize ferromagnetic Heisenberg spin-1/2 chains, and provide a versatile bottom-up assembly of robust spin centers in 1D as promising qubit platforms for quantum information processing. Furthermore, realizing JGNRs with asymmetric zigzag edge structures and different widths also enables the creation of 1D fully spin-polarized current channels with tunable bandgaps, crucial for the development of high-speed and energy-efficient carbon-based spintronics at the ultimate downscaling.

Method

In-solution and on-surface synthesis. For the synthesis of the precursor of 5-ZGNR, both branches of the Z-shape precursor are concurrently generated through the Suzuki coupling of 5,5'-dibromo-2,2'-diiodo-1,1'-biphenyl with methylphenyl boronic acid, then generating an ethynyl group *via* the cleavage of the triisopropylsilyl. Subsequent PtCl₃ catalysed cyclization of the ethynyl moiety produces two methylphenanthrene motifs connected by a C-C bond (precursor **3**), serving as branches to construct the zigzag edges. In contrast, for the precursor of JGNRs, one of the two methylphenanthrene branches is substituted by biphenyl and triphenyl groups by an additional step of Suzuki coupling. The synthetic procedures of the precursors are detailed in Supplementary Information. Au(111) single crystal (MaTeck GmbH) was cleaned by multiple cycles of Ar⁺ sputtering and annealing. Knudsen cell (MBE-Komponenten GmbH) was used for the deposition of precursor molecules onto clean Au(111) surfaces under ultrahigh vacuum conditions (base pressure, $<2 \times 10^{-10}$ mbar) for on-surface synthesis of product **1**. The precursor was sublimated at varying temperature for 1 minute to achieve a moderate coverage on Au(111). After the deposition of precursors, the sample was stepwise annealed at elevated temperatures as stated in the main text for 20 min to induce intramolecular dehydrogenation (Fig. S4).

STM/BR-STM/nc-AFM and dI/dV characterization. The experiments were conducted in Scienta Omicron LT-STM/AFM systems operated under ultrahigh vacuum (base pressure, $p < 2 \times 10^{-11}$ mbar) at a temperature of $T = 4.5$ K. All the BR-STM and nc-AFM images were taken in constant height mode with a CO functionalized tip. The microscope of Scienta Omicron was equipped with qPlus sensors S0.8 (see table I in ref. 38) with a resonance frequency of $f_0 = 39.646$ K Hz, a stiffness of 3600 N/m, and a quality factor of 119115. nc-AFM images were collected at a constant-height frequency modulation mode using an oscillation amplitude of $A = 20$ pm. The tip-sample distance with respect to an STM set point

is indicated in the figure caption for the corresponding AFM image. The images were analyzed and processed with Gwyddion software. The dI/dV spectra were collected using a standard lock-in technique with a modulated frequency of 479 Hz. The modulation voltages for individual measurements are provided in the corresponding figure captions. The STM tip was calibrated spectroscopically against the surface state of Au(111) substrate.

Computational Method. First-principles DFT calculations in the LSDA were performed using the Quantum Espresso packages.^{46,47} A supercell geometry was employed, with a 10 Å vacuum spacing placed in all non-periodic directions to prevent interaction between replicas. The atomic geometry was fully relaxed until all components of the forces on each atom were smaller than 0.01 eV/Å. A 100 Ry wavefunction energy cut-off, along with scalar relativistic and norm-conserving pseudopotentials for C and H, were used.^{48,49}

Acknowledgement

J. Lu acknowledges the support from MOE grants (MOE2019-T2-2-044, MOE T2EP50121-0008, MOE-T2EP10221-0005) and Agency for Science, Technology and Research (A*STAR) under its AME IRG Grant (Project715 No. M21K2c0113). S.G. Louie acknowledges the support from the U.S. National Science Foundation under grant number DMR-2325410, which provided all the theoretical topological formulation and analyses as well as the density functional theory calculations. H. Sakaguchi acknowledges the support from KAKENHI program No. 22H01891. T. Kojima acknowledges the support from KAKENHI program No. 23K04521. S. Song acknowledges the support from A*STAR under its AME YIRG Grant (M22K3c0094).

Competing interests

F.J.G. holds patents on the qPlus sensor. The other authors declare no competing interest.

Contributions

J. Lu supervised the project and organized the collaboration. S.S. and J. Lu conceived and designed the experiments. S.S. and Y.T. carried out the STM/nc-AFM measurements. Z.X., S.S., T.K. and H.S. synthesized the organic precursors. W.T, J.R., and S.G.L. conceived the

theoretical studies, performed the topological theory analyses, and carried out the DFT calculations. Y.H. and W.H. participate in the discussion. F.J.G. assisted in the optimization of the nc-AFM measurements and instrumentation. S.S., W.T., S.G.L. and J. Lu wrote the manuscript with inputs from all authors.

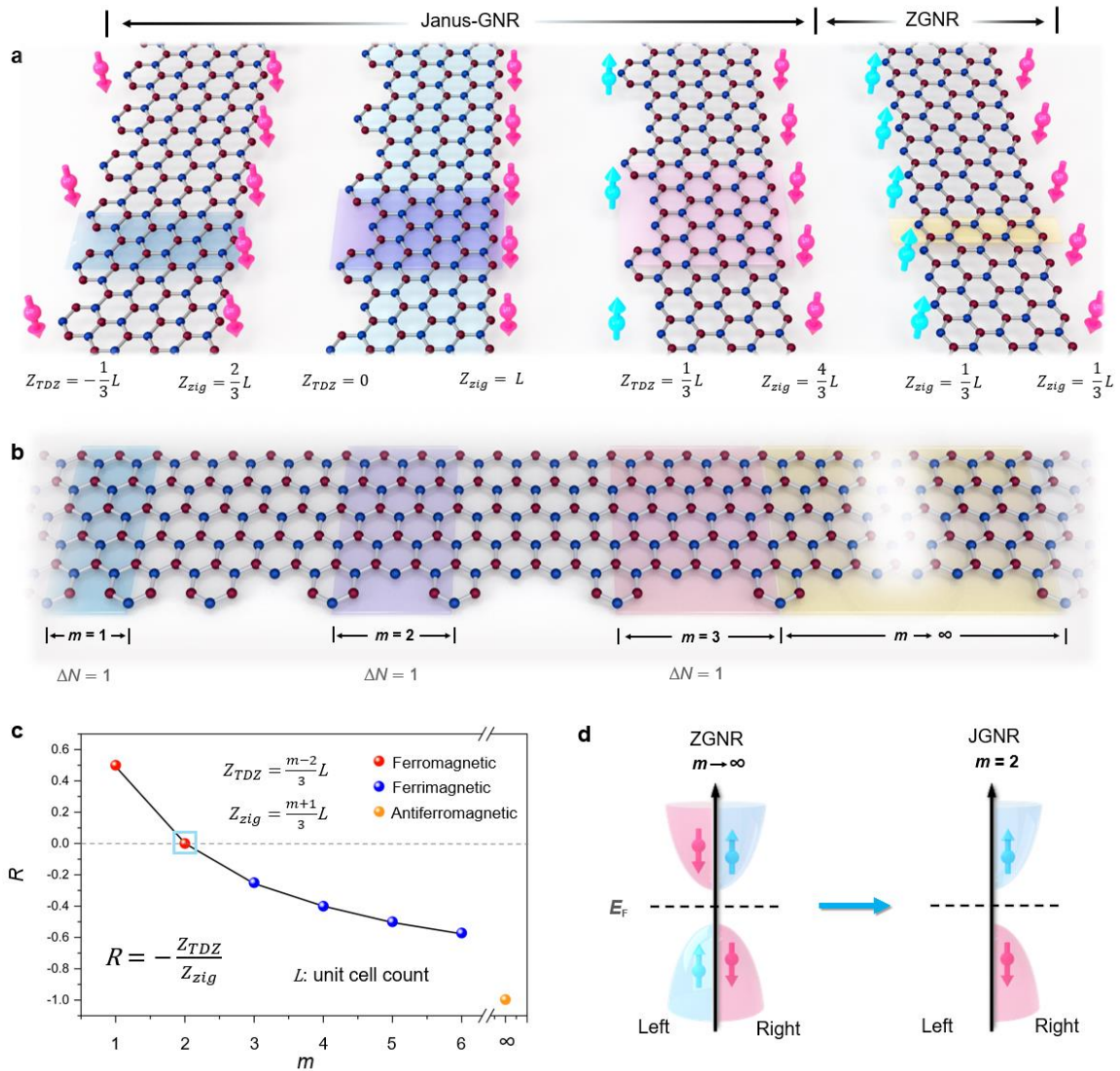


Figure 1| Design principle of JGNRs. a. Schematic illustration of JGNRs with various TDZ edges of different m values. Blue and red arrows represent spin-up and spin-down of edge states, respectively. The numbers at the bottom represent the CPI index of the corresponding TDZ (Z_{TDZ}) and intact zigzag (Z_{zig}) edges, where L is the number of repeated units along the zigzag direction (the repeated units are shaded by colors). **b.** The schematic diagram of the repeated unit of JGNRs, illustrating a gradual increase in “defective” site spacing between adjacent extra benzene rings, progressing from left to right: 1, 2, 3, and towards infinity (∞). The sublattice imbalance remains as $\Delta N = 1$ per repeated unit for all the cases except for $m = \infty$. **c.** The graph illustrates m -dependent magnetic orderings between two edges, which can be

described using the negative sign of the ratio of CPI index for the two edges in JGNRs (defined as $R = -\frac{Z_{TDZ}}{Z_{zig}}$). As m increases, R transform from positive to negative value, crossing 0 at $m = 2$. From Lieb's theorem and CPI theory, JGNR undergoes a transition from ferromagnetic to antiferromagnetic through a region of ferrimagnetic ordering. **d.** Schematic diagram of the spin-polarized band structure near the fundamental bandgap going from ZGNR ($m = \infty$, antiferromagnetic coupling between the two symmetric zigzag edges that are ferromagnetically ordered) to JGNR ($m = 2$, ferromagnetic order only at the single zigzag edge).

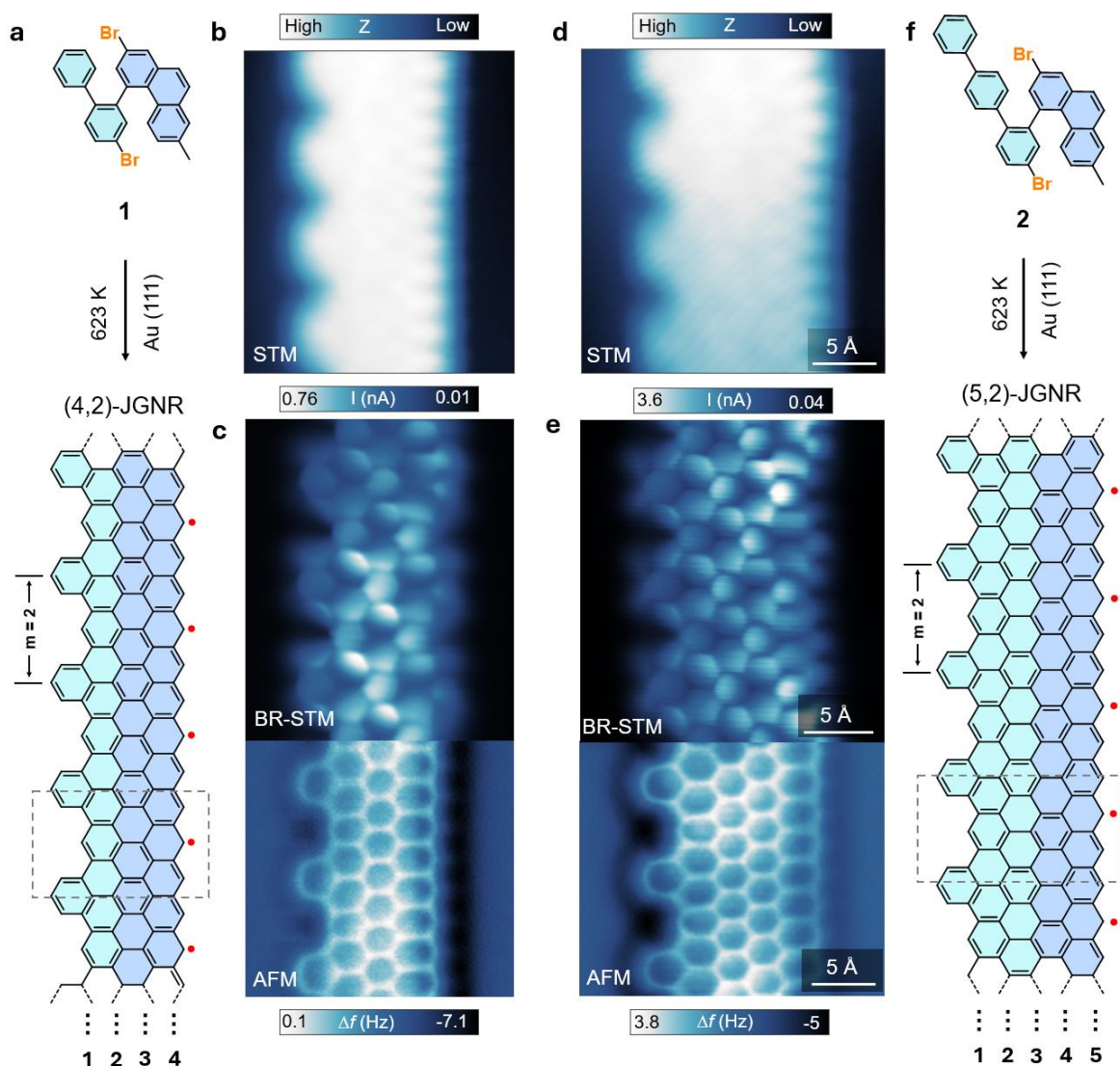


Figure 2 | On-surface synthesis and structural characterization of the JGNRs. a, On-surface synthetic strategy of (4,2)-JGNR. **b.** Constant current STM image of (4,2)-JGNR ($V_s = -800\text{mV}$, $I=100\text{pA}$) **c.** BR-STM image ($V_s = -10\text{ mV}$) and nc-AFM image ($V_s = 10\text{ mV}$)

of (4,2)-JGNR acquired at constant height mode using a qPlus sensor with a CO functionalized tip. **d.** Constant current STM image of (5,2)-JGNR ($V_s = -800\text{mV}$, $I = 100\text{pA}$). **e.** BR-STM image ($V_s = -10\text{ mV}$) and nc-AFM image ($V_s = 10\text{ mV}$) of the (5,2)-JGNR acquired at constant height mode using a qPlus sensor with a CO functionalized tip. **f.** On-surface synthetic strategy of (5,2)-JGNR.

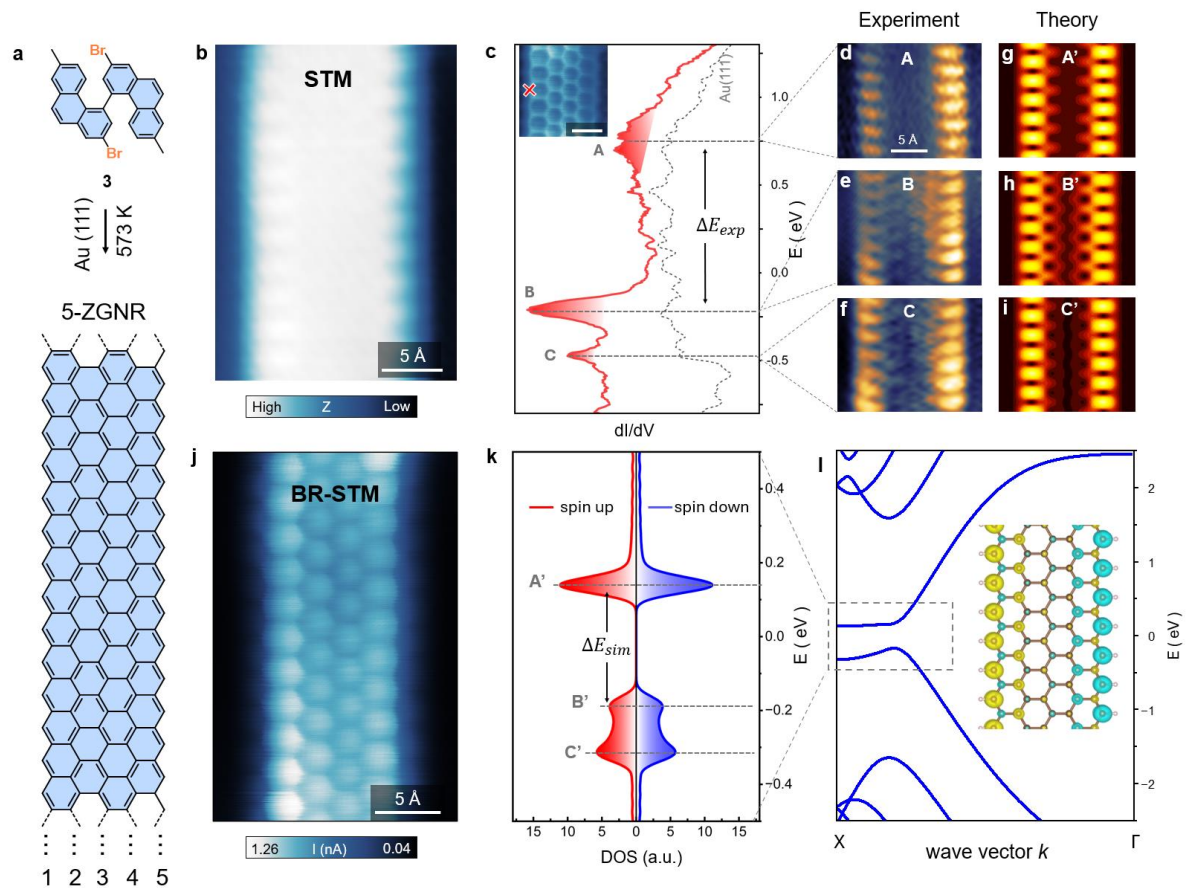


Figure 3| Fabrication and characterization of 5-ZGNR. **a.** On-surface synthetic strategy of 5-ZGNRs. **b.** Constant current STM image of the 5-ZGNR ($V_s = 10\text{ mV}$) **c.** dI/dV point spectroscopy of 5-ZGNR on Au(111) at the position marked in the inset panel (red cross). Dashed line shows the Au(111) reference spectrum ($V_{ac} = 20\text{ mV}$). Inset is the nc-AFM image acquired at constant height mode using a qPlus sensor with a CO functionalized tip ($V_s = 10\text{ mV}$). **d, e, f.** Constant-current dI/dV map recorded at a voltage bias of +750, -225 and -470 mV respectively. ($V_{ac} = 10\text{ mV}$). **g, h, f.** DFT-calculated LDOS at the energetic positions of A', B', and C' of the DOS spectrum as marked in panel **k**, respectively. LDOS are computed at a height of 4 Å above the atomic plane of the 5-ZGNR. **j.** BR-STM image of 5-ZGNR ($V_s = 10\text{ mV}$). **k.** DFT-calculated DOS of spin-up (red) and spin-down (blue) of 5-ZGNR

(broadened by 27 meV Gaussian). **l.** The DFT-calculated band structure of 5-ZGNR. Inset shows the calculated spin density distribution of a free-standing 5-ZGNR.

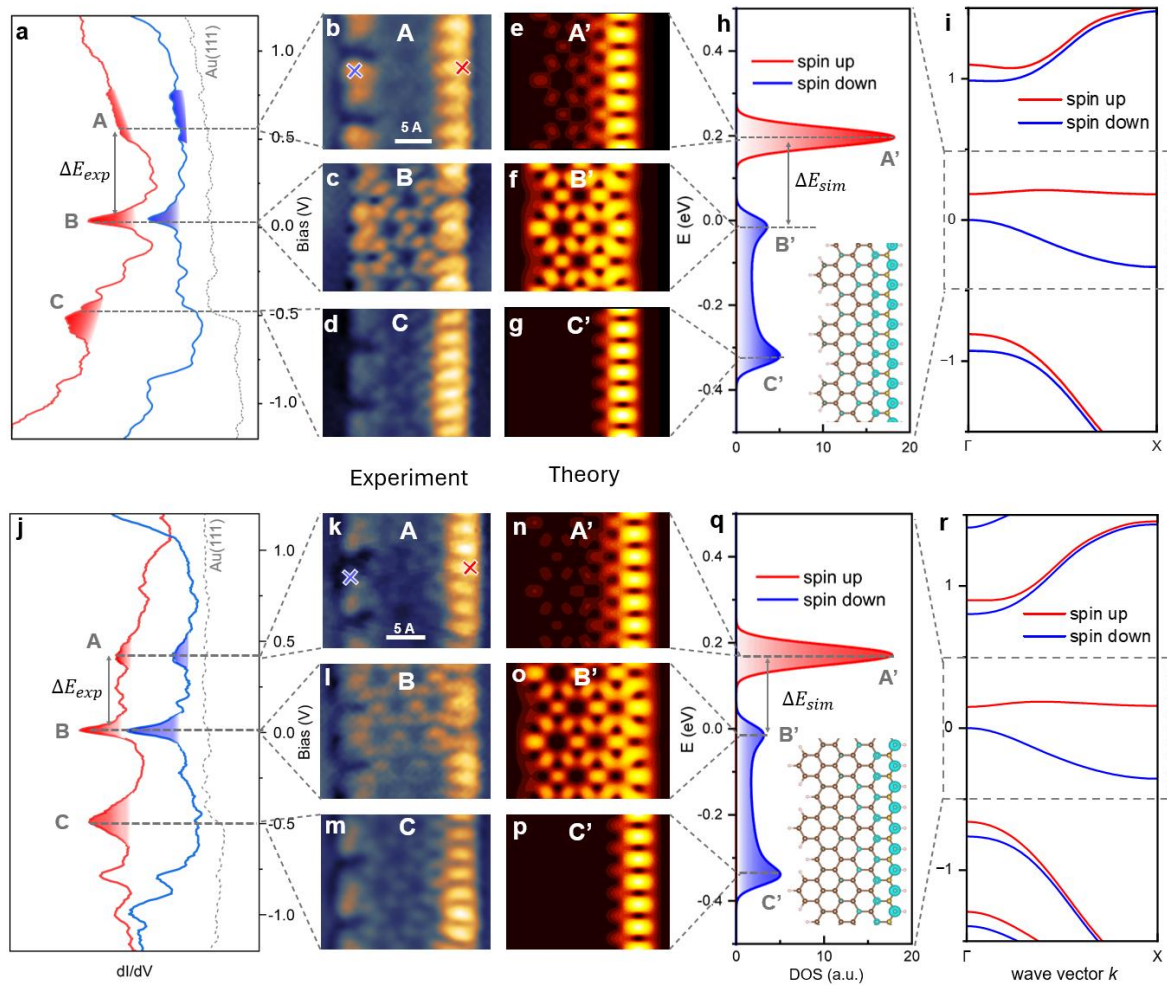


Figure 4| Electronic structure of JGNRs. **a.** dI/dV point spectroscopy of $(4,2)$ -JGNR on Au(111) at the corresponding colored position marked in panel **b** (red and blue cross). Dashed line shows the Au(111) reference spectrum ($V_{ac} = 20$ mV). **b, c, d.** Constant-current dI/dV maps recorded at voltage bias of +560, +48, and -492 mV, respectively ($V_{ac} = 10$ mV). **e, f, g.** DFT- calculated LDOS at the energetic positions of A' , B' , and C' marked in panel **h**, respectively. LDOS is computed at a height of 4 Å above the atomic plane of the $(4,2)$ -JGNR. **h.** DFT-calculated DOS of spin-up (red) and spin-down (down) of $(4,2)$ -JGNR (broadened by 27 meV Gaussian). Inset is the calculated spin density distribution of a free-standing $(4,2)$ -JGNR. **i.** The DFT calculated band structure for $(4,2)$ -JGNR. **j.** dI/dV point spectroscopy of $(5,2)$ -JGNR on Au(111) at the corresponding colored position marked in panel **k** (red and blue cross). Dashed line shows the Au(111) reference spectrum ($V_{ac} = 20$ mV). **k, l, m.**

Constant-current dI/dV map recorded at a voltage bias of +417, 11, and -500 mV, respectively ($V_{ac} = 10$ mV). **n, o, p.** Calculated DFT LDOS at the energetic positions of A', B', and C' marked in panel **q**, respectively. LDOS is computed at a height of 4 Å above the atomic plane of the (5,2)-JGNR. **q.** Calculated DFT DOS of spin-up (red) and spin-down (blue) of (5,2)-JGNR. Inset is the calculated spin density distribution of a free-standing (5,2)-JGNR. **r.** The DFT-calculated band structure of (5,2)-JGNR.

Reference

- 1 Ruffieux, P. *et al.* On-surface synthesis of graphene nanoribbons with zigzag edge topology. *Nature* **531**, 489-492 (2016).
- 2 Blackwell, R. E. *et al.* Spin splitting of dopant edge state in magnetic zigzag graphene nanoribbons. *Nature* **600**, 647-652 (2021).
- 3 Slota, M. *et al.* Magnetic edge states and coherent manipulation of graphene nanoribbons. *Nature* **557**, 691-695 (2018).
- 4 Lawrence, J. *et al.* Probing the magnetism of topological end states in 5-armchair graphene nanoribbons. *ACS nano* **14**, 4499-4508 (2020).
- 5 Fujita, M., Wakabayashi, K., Nakada, K. & Kusakabe, K. Peculiar localized state at zigzag graphite edge. *Journal of the Physical Society of Japan* **65**, 1920-1923 (1996).
- 6 Yang, L., Park, C.-H., Son, Y.-W., Cohen, M. L. & Louie, S. G. Quasiparticle energies and band gaps in graphene nanoribbons. *Physical review letters* **99**, 186801 (2007).
- 7 de Oteyza, D. G. & Frederiksen, T. Carbon-based nanostructures as a versatile platform for tunable π -magnetism. *Journal of Physics: Condensed Matter* **34**, 443001 (2022).
- 8 Yazyev, O. V. & Katsnelson, M. Magnetic correlations at graphene edges: basis for novel spintronics devices. *Physical review letters* **100**, 047209 (2008).
- 9 Magda, G. Z. *et al.* Room-temperature magnetic order on zigzag edges of narrow graphene nanoribbons. *Nature* **514**, 608-611 (2014).
- 10 Haldane, F. Excitation spectrum of a generalised Heisenberg ferromagnetic spin chain with arbitrary spin. *Journal of Physics C: Solid State Physics* **15**, L1309 (1982).
- 11 Trauzettel, B., Bulaev, D. V., Loss, D. & Burkard, G. Spin qubits in graphene quantum dots. *Nature Physics* **3**, 192-196 (2007).
- 12 Wang, H. *et al.* Graphene nanoribbons for quantum electronics. *Nature Reviews Physics* **3**, 791-802 (2021).
- 13 Lieb, E. H. Two theorems on the Hubbard model. *Physical review letters* **62**, 1201 (1989).
- 14 Cao, T., Zhao, F. & Louie, S. G. Topological phases in graphene nanoribbons: junction states, spin centers, and quantum spin chains. *Physical review letters* **119**, 076401 (2017).
- 15 Jiang, J. & Louie, S. G. Topology classification using chiral symmetry and spin correlations in graphene nanoribbons. *Nano letters* **21**, 197-202 (2020).
- 16 Hu, J., Zhou, S., Sun, Y., Fang, X. & Wu, L. Fabrication, properties and applications of Janus particles. *Chemical Society Reviews* **41**, 4356-4378 (2012).

- 17 Li, R., Cheng, Y. & Huang, W. Recent progress of Janus 2D transition metal
chalcogenides: from theory to experiments. *Small* **14**, 1802091 (2018).
- 18 Zhang, L. *et al.* Janus graphene from asymmetric two-dimensional chemistry. *Nature
Communications* **4**, 1443 (2013).
- 19 Lu, A.-Y. *et al.* Janus monolayers of transition metal dichalcogenides. *Nature
nanotechnology* **12**, 744-749 (2017).
- 20 Zhang, J. *et al.* Janus monolayer transition-metal dichalcogenides. *ACS nano* **11**,
8192-8198 (2017).
- 21 Zhang, L. *et al.* Janus two-dimensional transition metal dichalcogenides. *Journal of
Applied Physics* **131** (2022).
- 22 Sun, Q. *et al.* Coupled spin states in armchair graphene nanoribbons with asymmetric
zigzag edge extensions. *Nano letters* **20**, 6429-6436 (2020).
- 23 Rizzo, D. J. *et al.* Inducing metallicity in graphene nanoribbons via zero-mode
superlattices. *Science* **369**, 1597-1603 (2020).
- 24 Son, Y.-W., Cohen, M. L. & Louie, S. G. Half-metallic graphene nanoribbons. *Nature*
444, 347-349 (2006).
- 25 Zhang, D.-B. & Wei, S.-H. Inhomogeneous strain-induced half-metallicity in bent
zigzag graphene nanoribbons. *npj Computational Materials* **3**, 32 (2017).
- 26 Lee, Y.-L., Kim, S., Park, C., Ihm, J. & Son, Y.-W. Controlling half-metallicity of
graphene nanoribbons by using a ferroelectric polymer. *Acs Nano* **4**, 1345-1350
(2010).
- 27 Kan, E.-j., Li, Z., Yang, J. & Hou, J. Half-metallicity in edge-modified zigzag
graphene nanoribbons. *Journal of the American Chemical Society* **130**, 4224-4225
(2008).
- 28 Ovchinnikov, A. A. Multiplicity of the ground state of large alternant organic
molecules with conjugated bonds: (Do Organic Ferromagnetics Exist?). *Theoretica
chimica acta* **47**, 297-304 (1978).
- 29 Ugeda, M. M., Brihuega, I., Guinea, F. & Gómez-Rodríguez, J. M. Missing atom as a
source of carbon magnetism. *Physical Review Letters* **104**, 096804 (2010).
- 30 Palacios, J. J., Fernández-Rossier, J. & Brey, L. Vacancy-induced magnetism in
graphene and graphene ribbons. *Physical Review B* **77**, 195428 (2008).
- 31 Song, S. *et al.* On-surface synthesis of graphene nanostructures with π -magnetism.
Chemical Society Reviews **50**, 3238-3262 (2021).
- 32 Sakaguchi, H., Song, S., Kojima, T. & Nakae, T. Homochiral polymerization-driven
selective growth of graphene nanoribbons. *Nature Chemistry* **9**, 57-63 (2017).
- 33 Kojima, T. *et al.* Vectorial On-Surface Synthesis of Polar 2D Polymer Crystals.
Advanced Materials Interfaces **10**, 2300214 (2023).
- 34 Kojima, T. *et al.* Molecular-Vapor-Assisted Low-Temperature Growth of Graphene
Nanoribbons. *The Journal of Physical Chemistry C* **127**, 10541-10549 (2023).
- 35 Piquero-Zulaica, I. *et al.* Deceptive orbital confinement at edges and pores of carbon-
based 1D and 2D nanoarchitectures. *Nature Communications* **15**, 1062 (2024).
- 36 Li, J. *et al.* Uncovering the triplet ground state of triangular graphene nanoflakes
engineered with atomic precision on a metal surface. *Physical Review Letters* **124**,
177201 (2020).
- 37 Li, J. *et al.* Topological phase transition in chiral graphene nanoribbons: from edge
bands to end states. *Nature communications* **12**, 5538 (2021).
- 38 Giessibl, F. J. The qPlus sensor, a powerful core for the atomic force microscope.
Review of scientific instruments **90** (2019).
- 39 Gross, L., Mohn, F., Moll, N., Liljeroth, P. & Meyer, G. The chemical structure of a
molecule resolved by atomic force microscopy. *Science* **325**, 1110-1114 (2009).

- 40 Kinikar, A. *et al.* On-Surface Synthesis of Edge-Extended Zigzag Graphene
Nanoribbons. *Advanced Materials* **35**, 2306311 (2023).
- 41 Neaton, J. B., Hybertsen, M. S. & Louie, S. G. Renormalization of molecular
electronic levels at metal-molecule interfaces. *Physical review letters* **97**, 216405
(2006).
- 42 Li, J. *et al.* Single spin localization and manipulation in graphene open-shell
nanostructures. *Nature communications* **10**, 200 (2019).
- 43 Nguyen, G. D. *et al.* Atomically precise graphene nanoribbon heterojunctions from a
single molecular precursor. *Nature nanotechnology* **12**, 1077-1082 (2017).
- 44 Chen, Y.-C. *et al.* Molecular bandgap engineering of bottom-up synthesized graphene
nanoribbon heterojunctions. *Nature nanotechnology* **10**, 156-160 (2015).
- 45 Hybertsen, M. S. & Louie, S. G. Electron correlation in semiconductors and
insulators: Band gaps and quasiparticle energies. *Physical Review B* **34**, 5390 (1986).
- 46 Giannozzi, P. *et al.* QUANTUM ESPRESSO: a modular and open-source software
project for quantum simulations of materials. *Journal of physics: Condensed matter*
21, 395502 (2009).
- 47 Giannozzi, P. *et al.* Advanced capabilities for materials modelling with Quantum
ESPRESSO. *Journal of physics: Condensed matter* **29**, 465901 (2017).
- 48 Hamann, D. Erratum: optimized norm-conserving vanderbilt pseudopotentials [Phys.
Rev. B 88, 085117 (2013)]. *Physical Review B* **95**, 239906 (2017).
- 49 Van Setten, M. J. *et al.* The PseudoDojo: Training and grading a 85 element
optimized norm conserving pseudopotential table. *Computer Physics Communications*
226, 39-54 (2018).